Supporting Information

Precise site occupation of Zn^{2+} in Rb_2CuBr_3 to regulate exciton recombination for violet luminescence

Jiajia Wang, [a, b] Rui Zhou, [a, b] Jie Ren, [a, b] Jingrui Guo, [a, b] Jianyong Zhang, [c] Jing Guo, [a, b*] Na Zhang, [a, b*] Yufeng Liu, [a, b] Yongzheng Fang [a, b*]

[a] Faculty of Materials Technology, Shanghai Institute of Technology, Shanghai, 201418, People's Republic of China

[b] Shanghai Engineering Research Center of Photodetection Materials and Devices, Shanghai Institute of Technology, Shanghai 201418, People's Republic of China

[c] School of Chemical and Environmental Engineering, Shanghai Institute of Technology, Shanghai, 201418, People's Republic of China

[*] E-mail: guoj@sit.edu.cn, nzhang@sit.edu.cn, fyz1003@sina.com

1. Supplementary sections

1.1 Computational modeling based on density functional theory

1.2 Fabrication of Violet LED

2. Supplementary figures

Figure S1. Schematic illustration of the experimental synthesis.

Figure S2. Charge density difference isosurface maps. Orange: electron accumulation; Green: electron depletion. (a) Pristine Rb_2CuBr_3 (reference), (b) Rb_2CuBr_3:0.3Zn^{2+}.

Figure S3. Rb 3d spectrum with the characteristic main peaks (Rb $3d_{5/2}$ and Rb $3d_{3/2}$) and satellite features.

Figure S4. The fitting curve of Rb_2CuBr_3 and Rb_2CuBr_3:0.3 Zn^{2+} in $|\chi(k)|$ space.

Figure S5. The fitting curve of Cu_2O in $|\chi(k)|$ and $|\chi(R)|$ space.

Figure S6. Wavelet transform diagram of Cu_2O.

Figure S7. XPS curve for Zn 2p.

Figure S8. Comparison of the experimental XRD patterns for pristine and Rb_2CuBr_3:0.3Zn^{2+}.

Figure S9. EDS analysis of Rb_2CuBr_3:0.3Zn^{2+}.

Figure S10. Bandgap analysis of Rb_2CuBr_3 on DFT calculations (Dashed lines: VBM/CBM positions). (a) Rb_2CuBr_3. (b) Rb_2CuBr_3:Zn^{2+}.

Figure S11. The computational band gap values of Rb_2CuBr_3:xZn^{2+}.

Figure S12. Normalized PLE spectra of Rb_2CuBr_3 monitored at 340-385 nm, PL spectra under 240-330 nm irradiation: (a) Rb_2CuBr_3, (b) Rb_2CuBr_3:0.1Zn^{2+}, (c) Rb_2CuBr_3:0.2Zn^{2+}, (d) Rb_2CuBr_3:0.3Zn^{2+}, (e) Rb_2CuBr_3:0.4Zn^{2+}.

Figure S13. Photoluminescence photographs of Rb_2CuBr_3:xZn^{2+} upon 302 nm

excitation.

Figure S14. The PL intensity of stability evolution of Rb_2CuBr_3 and Rb_2CuBr_3:0.3 Zn^{2+} under ambient storage.

Figure S15. PL decay curves of (a) Rb_2CuBr_3:0.1 Zn^{2+}, (b) Rb_2CuBr_3:0.2 Zn^{2+}, (c) Rb_2CuBr_3:0.4 Zn^{2+}.

Figure S16. Packaging of a portable device powered by a battery-connected LED.

3. Supplementary table

Table S1. Main fitting results of the fit performed on the k^2-Weighted EXAFS spectra for Rb_2CuBr_3, and Rb_2CuBr_3:0.3 Zn^{2+}.

Table S2. The correlation between the feeding ratio and the actual ratio of Zn/Cu.

Table S3. k_r and k_{nr} recombination rates during the doping process.

Table S4. Summary of the device performance of violet LED performance.

1. Supplementary sections

1.1 Computational modeling based on density functional theory

This study employed the Vienna Ab-initio Simulation Package (VASP) 5.4.4[1] to conduct DFT calculations. The Perdew-Burke-Ernzerhof (PBE) functional within the generalized gradient approximation (GGA) framework[2] was selected as the exchange-correlation functional. This functional has been widely validated for reliably predicting the crystal structure, electronic band gap, defect formation energy, and relative energies of halide perovskites,[3] and is suitable for doping configuration screening.

The calculations utilized the Projector Augmented Wave (PAW) pseudopotential,[4] with a plane-wave cutoff energy of 500 eV (verified to have energy fluctuations < 1 meV)/atom). The Brillouin zone integration was performed using a 5×5×1 Monkhorst-Pack k-grid centered at the Γ point (verified to ensure energy convergence to 1 meV through density testing). A 15 Å vacuum layer was set in the non-periodic direction (verified to have interlayer interaction energy < 1 meV through thickness testing). All atomic positions were fully relaxed until the energy change was ≤ 1×10^{-6} eV and the atomic force was ≤ 0.01 eV/A. Additionally, DFT-D3[5] dispersion correction (Becke-Jonson damping) was introduced to accurately describe van der Waals interactions.

Based on the aforementioned static calculations, we computed the band structures of both undoped and Zn-doped Rb_2CuBr_3, analyzed the density of states (DOS) at the doping sites, and evaluated the formation energies across various doping configurations. The Fermi level of pure Rb_2CuBr_3 is taken as the reference zero point for the band structure and DOS. To investigate the feasibility of doping and substitution

at various lattice sites, the formation energy was calculated using the following equations[6]:

$$E_{1\,form}^{doped} = E_{total}(Zn\ doped) - [E_{total}(Pure) + \mu_{Zn} - \mu_{Rb}] \quad (1)$$

$$E_{2\,form}^{doped} = E_{total}(Zn\ doped) - [E_{total}(Pure) + \mu_{Zn} - \mu_{Cu}] \quad (2)$$

$$E_{form}^{int} = E_{total}(X_{int}) - [E_{total}(Pure) + \mu_{x}] \quad (3)$$

Where E_{form}^{doped} and E_{form}^{int} represent doping formation energy and interstitial formation energy respectively. E_{total}(Zn doped) and E_{total}(X_{int}) are respectively the total energies containing Zn dopant and X interstitial. E_{total} (pure) is the total energy of an undoped Rb_2CuBr_3. μ_{Rb}, μ_{Cu} and μ_{Zn} are the chemical potential energies of Rb, Cu and Zn atoms, respectively.

1.2 Fabrication of violet LED

The prepared violet-blue emitting Rb_2CuBr_3:0.3Zn^{2+} perovskite material was coated onto a 295 nm UV chip for violet LED fabrication. Optical characterization of the violet-blue LED was performed with an LED analyzer (HP9000) across a range of drive currents (mA). Subsequently, integrating the packaged chip with a portable power supply allows for the fabrication of a portable LED device.

2. Supplementary figures

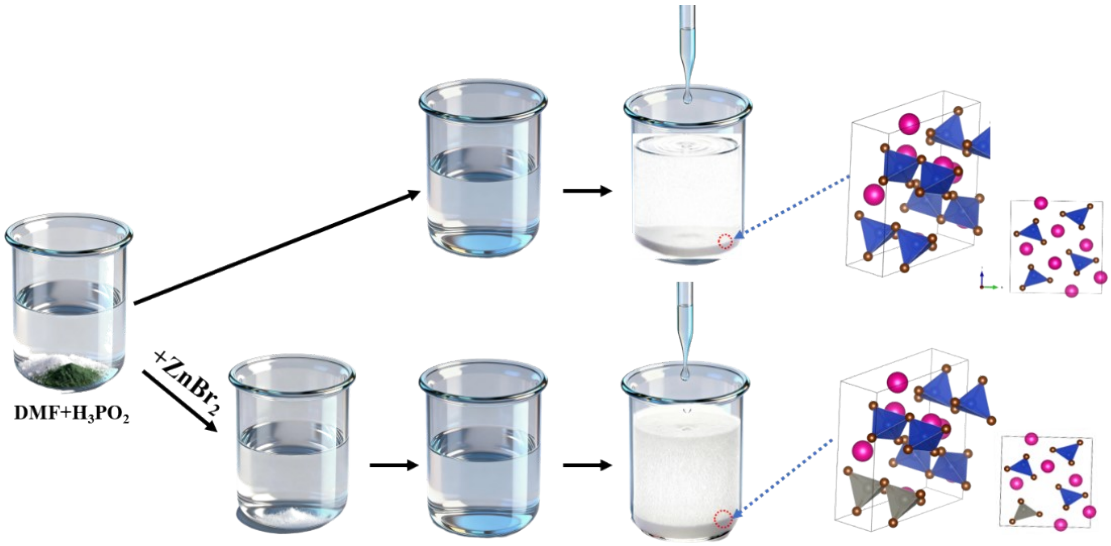

Figure S1. Schematic illustration of the experimental synthesis.

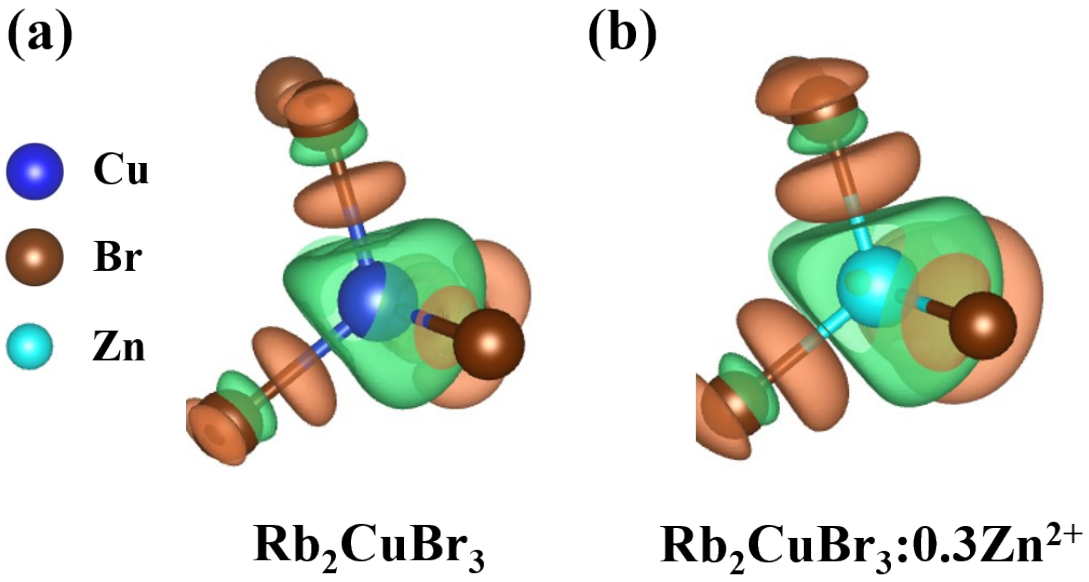

Figure S2 Charge density difference isosurface maps. orange: electron accumulation; green: electron depletion. (a) Pristine Rb_2CuBr_3 (reference), (b) Rb_2CuBr_3:0.3Zn^{2+}.

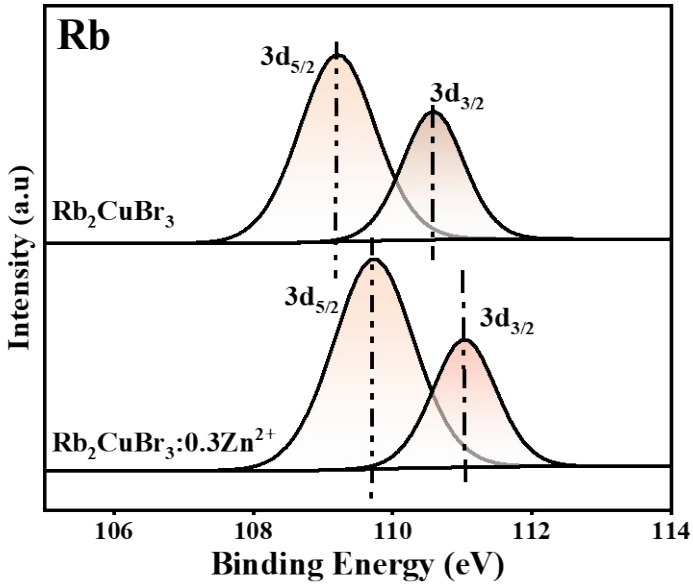

Figure S3. Rb 3d spectrum with the characteristic main peaks (Rb $3d_{5/2}$ and Rb $3d_{3/2}$) and satellite features.

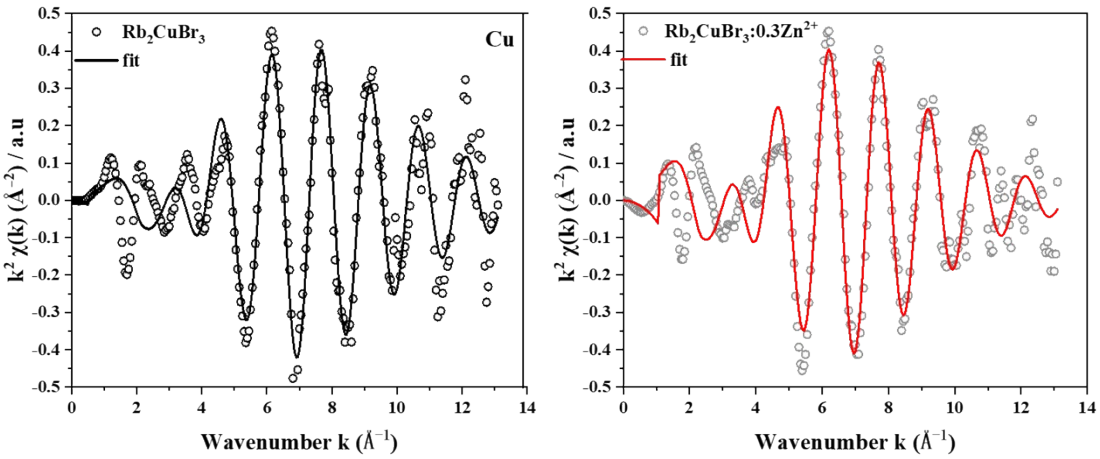

Figure S4. The fitting curve of Rb_2CuBr_3 and Rb_2CuBr_3:0.3Zn^{2+} in |χ(k)| space.

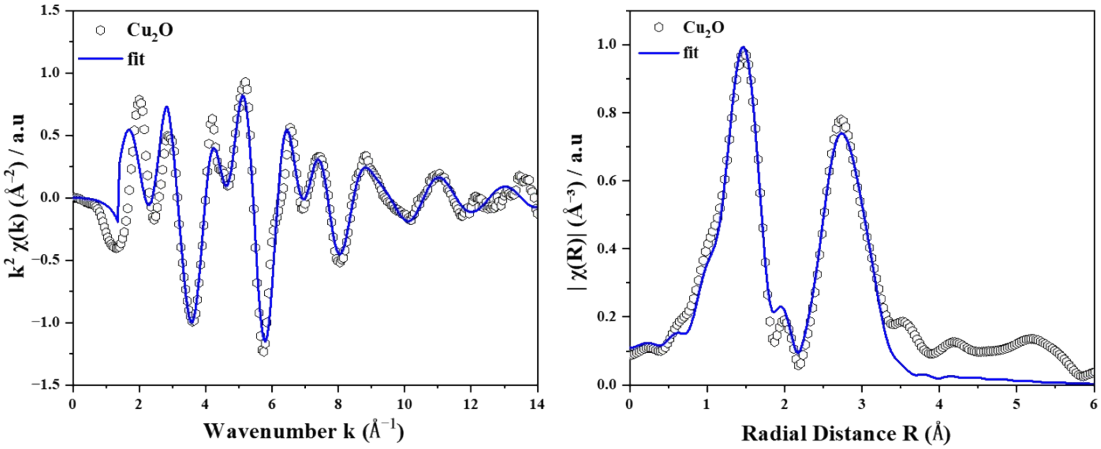

Figure S5. The fitting curve of Cu_2O in |χ(k)| and |χ(R)| space.

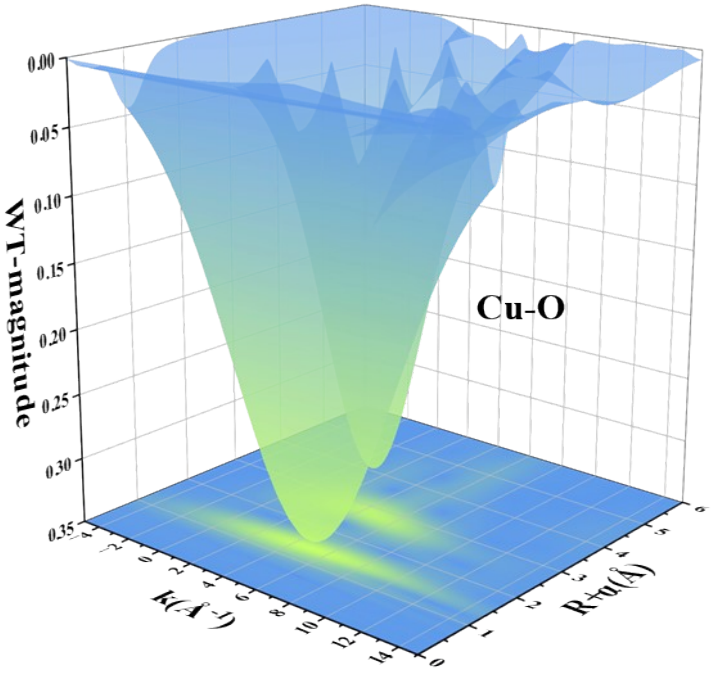

Figure S6. Wavelet transform diagram of Cu_2O.

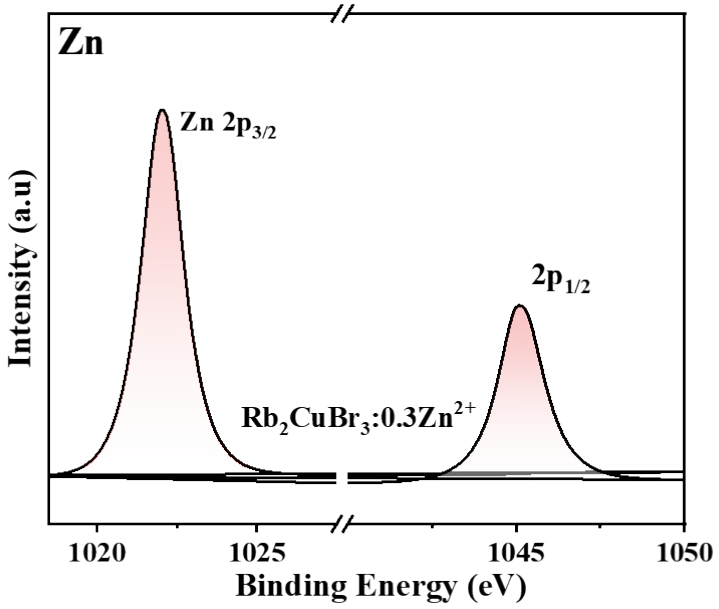

Figure S7. XPS curve for Zn 2p.

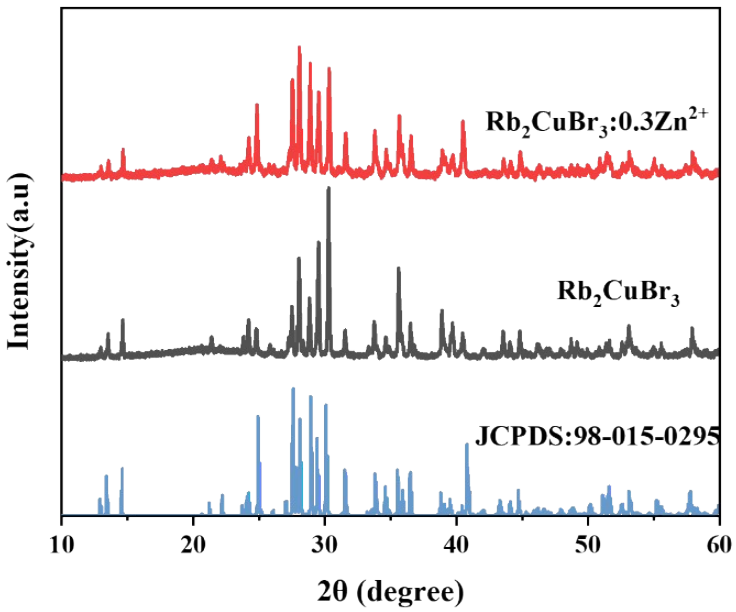

Figure S8. Comparison of the experimental XRD patterns for pristine and Rb_2CuBr_3:0.3Zn^{2+}.

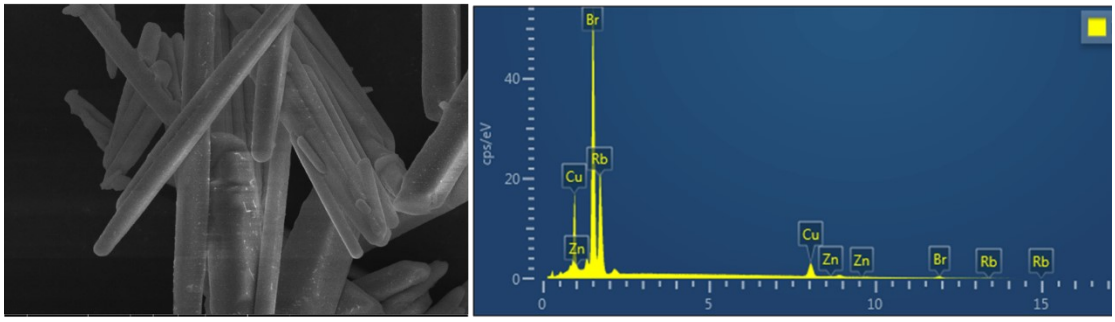

Figure S9. EDS analysis of Rb_2CuBr_3:0.3Zn^{2+}.

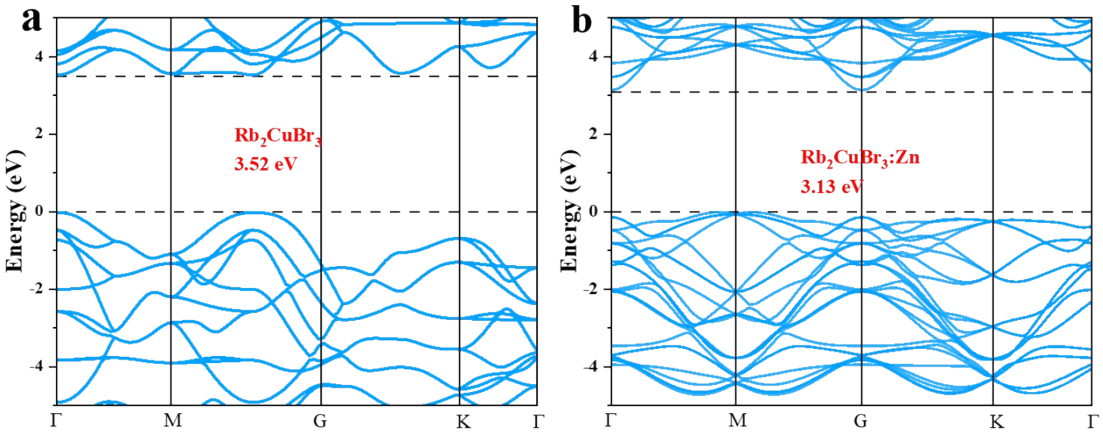

Figure S10. Bandgap analysis of Rb_2CuBr_3 on DFT calculations (Dashed lines: VBM/CBM positions). (a) Rb_2CuBr_3. (b) Rb_2CuBr_3:0.25Zn^{2+}.

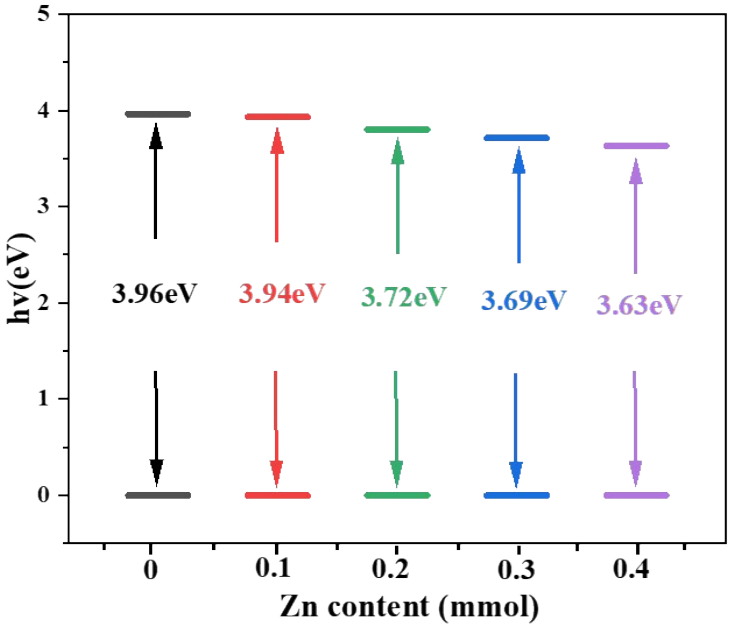

Figure S11. The computational band gap values of Rb_2CuBr_3:xZn^{2+}.

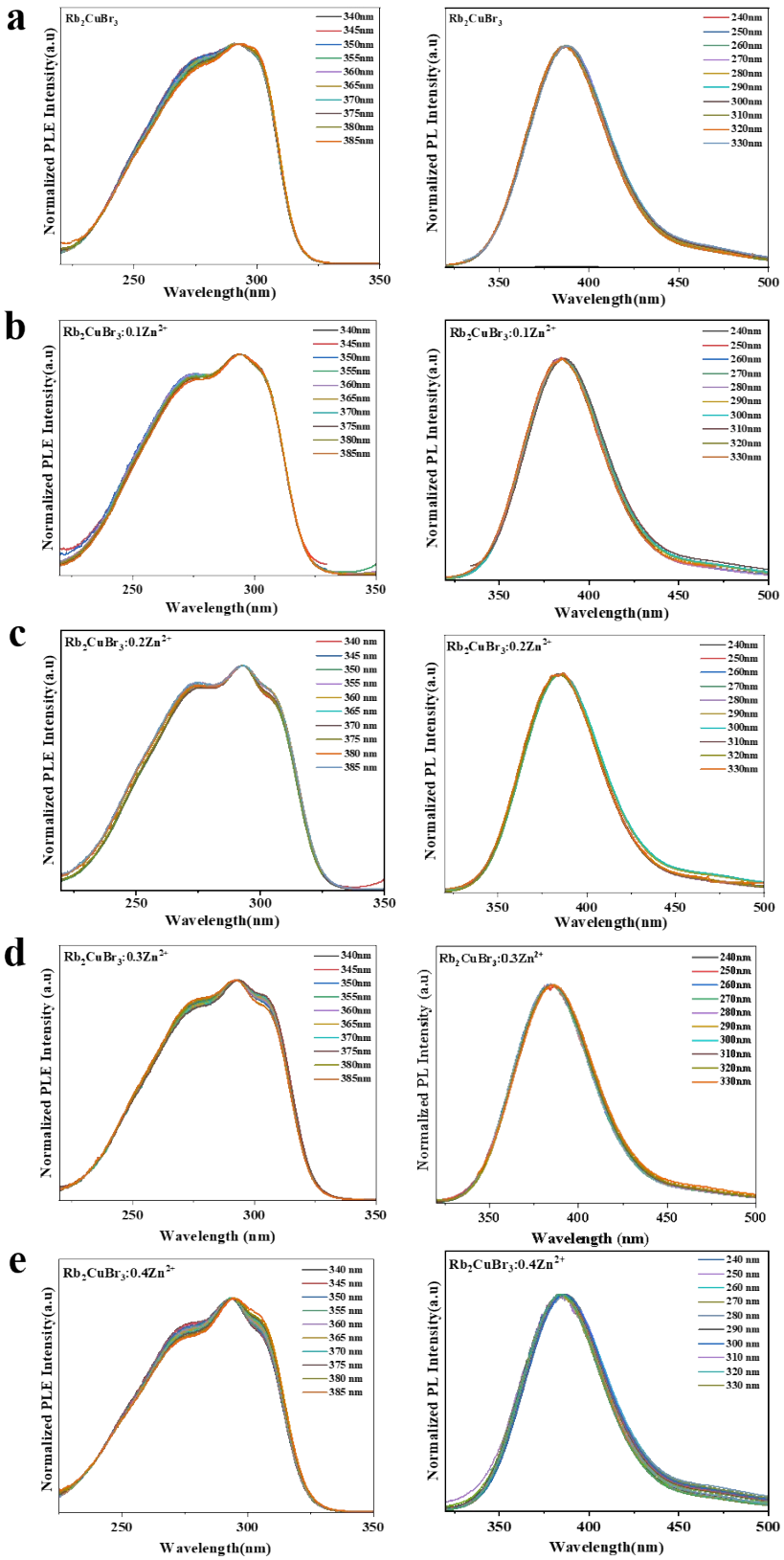

Figure S12. Normalized PLE spectra of Rb_2CuBr_3 monitored at 340-385 nm, PL spectra under 240-330 nm irradiation: (a) Rb_2CuBr_3, (b) Rb_2CuBr_3:0.1Zn^{2+}, (c) Rb_2CuBr_3:0.2Zn^{2+}, (d) Rb_2CuBr_3:0.3Zn^{2+}, (e) Rb_2CuBr_3:0.4Zn^{2+}.

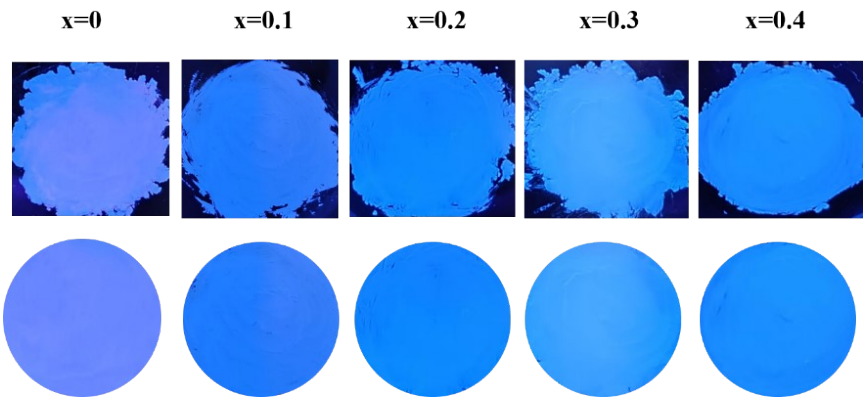

Figure S13. Photoluminescence photographs of Rb_2CuBr_3:xZn^{2+} upon 302 nm excitation.

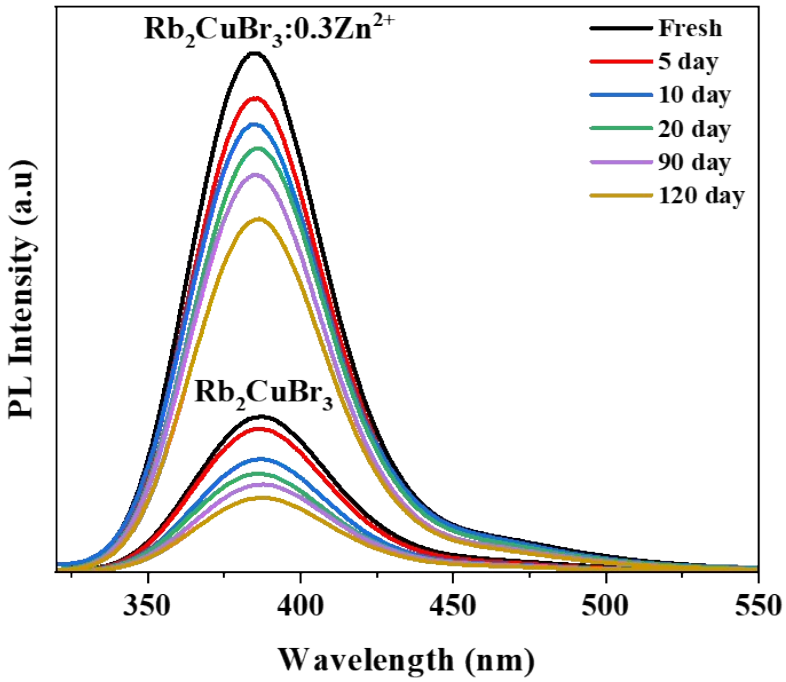

Figure S14. The PL intensity of stability evolution of Rb_2CuBr_3 and Rb_2CuBr_3:0.3Zn^{2+} under ambient storage.

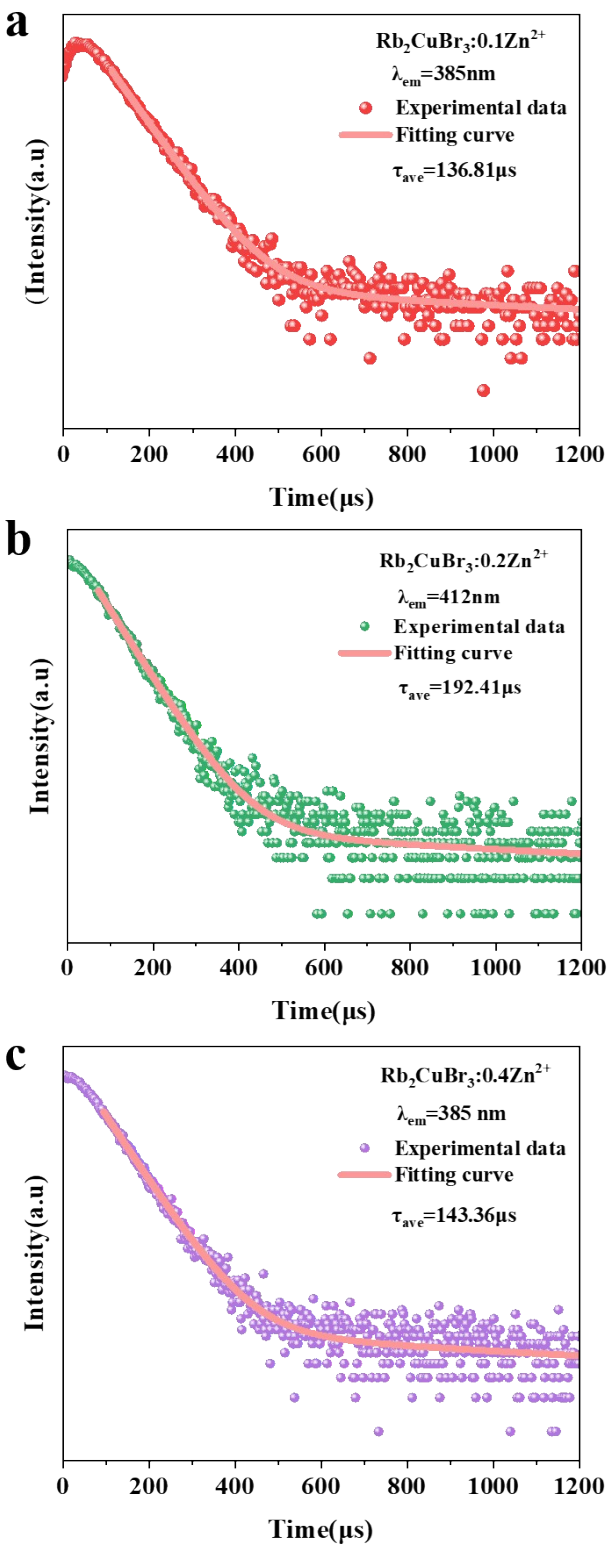

Figure S15. PL decay curves of (a) Rb_2CuBr_3:0.1Zn^{2+}, (b) Rb_2CuBr_3:0.2Zn^{2+}, (c) Rb_2CuBr_3:0.4 Zn^{2+}.

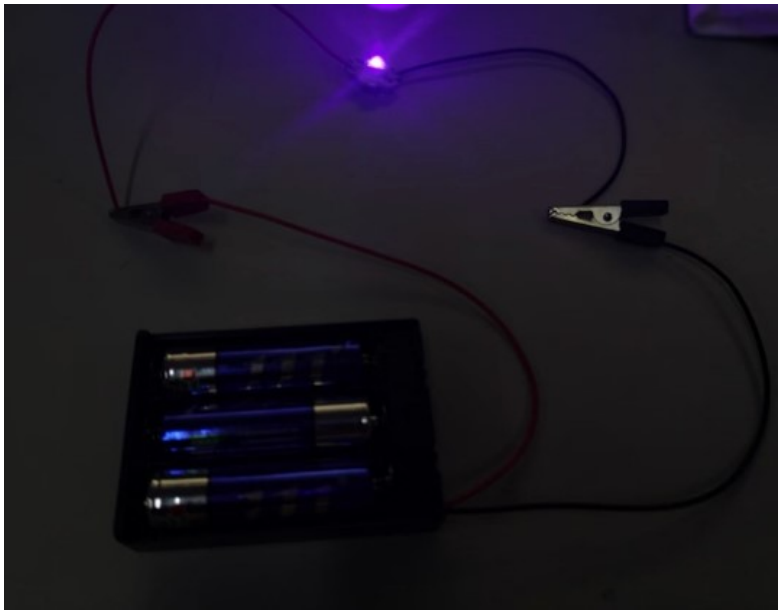

Figure S16. Packaging of a portable device powered by a battery-connected LED.

3. Supplementary table

Table S1. Main fitting results of the fit performed on the k^2-weighted EXAFS spectra forRb_2CuBr_3, and Rb_2CuBr_3:0.3 Zn^{2+}.

Sample	Path	CN[a]	R (Å) [b]	σ^2 (Å^2) [c]	ΔE_0 (eV) [d]	R factor[e]
Rb_2CuBr_3	Cu-Br	3.9±0.1	2.56±0.01	0.0094±0.0012	1.1±1.8	0.0123
Rb_2CuBr_3:0.3Zn^{2+}	Cu-Br	4.1±0.1	2.44±0.01	0.0125±0.0010	2.2±1.3	0.0060

[a]*CN*: coordination numbers; [b]*R*: bond distance; [c]σ^2: Debye-Waller factors; [d]ΔE_0: the inner potential correction. [e]*R* factor: goodness of fit.

Table S2. The correlation between the feeding ratio and the actual ratio of Zn/Cu.

Feeding amount of $ZnBr_2$ (mmol)	Feeding ratio of Zn/Cu (%)	Actual Zn (mg/L)	Actual Cu (mg/L)	Actual ratio of Zn/Cu (%)	Actual/feeding Zn amount (%)
0.1	10	54.88	593.03	9.3	92.5
0.2	20	88.78	507.19	17.5	87.5
0.3	30	120.09	486.36	24.7	82.3
0.4	40	135.35	486.25	27.8	69.6

Table S3. k_r and k_{nr} recombination rates during the doping process.

Sample	τ ($\times 10^{-6}$ s)	PLQY (%)	k_r (s^{-1})	k_{nr} (s^{-1})
Rb_2CuBr_3	126.20	51.4	4073	3851
Rb_2CuBr_3:0.1Zn^{2+}	136.81	53.6	3917	3391
Rb_2CuBr_3:0.2Zn^{2+}	194.41	64.6	3322	1821
Rb_2CuBr_3:0.3Zn^{2+}	254.99	70.6	2773	1149
Rb_2CuBr_3:0.4Zn^{2+}	143.36	63.1	4401	2574

Table S4. Summary of the device performance of violet LED performance.

Emission materials	$EL_{\lambda max}$ (nm)	PLQY (%)	EQE_{max} (%)
PEA_2PbBr_4 film[7]	410	10	0.04
PEA_2PbBr_4 NPs[8]	410	15-20	0.31
$Cs_3Sb_2Br_9$ QD[9]	408	51.2	0.206
Rb_2CuBr_3:0.3Zn^{2+}	385	70.6	0.22

4. Reference

[1] H. Wang, Y. C. Gan, H. Y. Geng and X.-R. Chen, *Comput. Phys. Commun.*, 2022, 281, 108495.

[2] A. V. Ivanov, A. Patterson, M. Bothe, C. Sünderhauf, B. K. Berntson, J. J. Mortensen, M. Kuisma, E. Campbell and R. Izsák, *J. Chem. Theory Comput.*, 2025, 21, 7360.

[3] P. E. Blöchl, *Phys. Rev. B*, 1994, 50, 17953.

[4] E. W. Caetano, J. B. Silva, C. H. Bruno, E. L. Albuquerque, B. P. e Silva, R. C. dos Santos, A. M. Teixeira and V. N. Freire, *J. Mol. Struct.*, 2024, 1300, 137228.

[5] I. U. Nabi Lone, M. M. Sheik Sirajuddeen, S. B. Mohamed and S. Khalid, *Mater. Chem. Phys.*, 2021, 260, 124159.

[6] Z.-J. Yong, S.-Q. Guo, J.-P. Ma, J.-Y. Zhang, Z.-Y. Li, Y.-M. Chen, B.-B. Zhang, Y. Zhou, J. Shu, J.-L. Gu, L.-R. Zheng, O. M. Bakr and H.-T. Sun, *J. Am. Chem. Soc.*, 2018, 140, 9942.

[7] L. Bai, S. Wang, Y. Zhang, K. Zhang, H. Li, K. Ou and L. Yi, *J. Lumin.*, 2020, 226, 117422.

[8] W. Deng, X. Jin, Y. Lv, X. Zhang, X. Zhang and J. Jie, *Adv. Funct. Mater.*, 2019, 29, 1903861.

[9] Z. Ma, Z. Shi, D. Yang, F. Zhang, S. Li, L. Wang, D. Wu, Y. Zhang, G. Na, L. Zhang, X. Li, Y. Zhang and C. Shan, *ACS Energy Lett.*, 2019, 5, 385.